INTERNATIONAL JOURNAL FOR NUMERICAL METHODS IN FLUIDS
Int. J. Numer. Meth. Fluids (2010)
Published online in Wiley InterScience (www.interscience.wiley.com). DOI: 10.1002/fld.2366

Curvilinear finite elements for Lagrangian hydrodynamics

V. A. Dobrev[1], T. E. Ellis[2], Tz. V. Kolev[1] and R. N. Rieben[3,*,†]

[1]*Center for Applied Scientific Computing, Lawrence Livermore National Laboratory, CA, U.S.A.*
[2]*Department of Aerospace Engineering, California Polytechnic State University, CA, U.S.A.*
[3]*Weapons and Complex Integration, Lawrence Livermore National Laboratory, CA, U.S.A.*

SUMMARY

We have developed a novel high-order, energy conserving approach for solving the Euler equations in a moving Lagrangian frame, which is derived from a general finite element framework. Traditionally, such equations have been solved by using continuous linear representations for kinematic variables and discontinuous constant fields for thermodynamic variables; this is the so-called staggered grid hydro (SGH) method. From our general finite element framework, we can derive several specific high-order discretization methods and in this paper we introduce a curvilinear finite element method which uses continuous bi-quadratic polynomial bases (the Q_2 isoparametric elements) to represent the kinematic variables combined with discontinuous (mapped) bi-linear bases to represent the thermodynamic variables. We consider this a natural generalization of the SGH approach and show that under simplifying low-order assumptions, we exactly recover the classical SGH method. We review the key parts of the discretization framework and demonstrate several practical advantages to using curvilinear finite elements for Lagrangian shock hydrodynamics, including: the ability to more accurately capture geometrical features of a flow region, significant improvements in symmetry preservation for radial flows, sharper resolution of a shock front for a given mesh resolution including the ability to represent a shock within a single zone and a substantial reduction in mesh imprinting for shock waves that are not aligned with the computational mesh. Copyright © 2010 John Wiley & Sons, Ltd.

Received 13 January 2010; Revised 27 April 2010; Accepted 27 April 2010

KEY WORDS: hydrodynamics; compressible flow; hyperbolic partial differential equations; Lagrangian methods; finite element methods; variational methods; high-order methods; curvilinear meshes

1. INTRODUCTION AND MOTIVATION

Our goal is to improve the traditional staggered grid hydro (SGH) algorithms used to solve the Euler equations in multi-material arbitrary Lagrangian–Eulerian (ALE) codes with respect to: symmetry preservation and mesh imprinting, total energy conservation, artificial viscosity treatment and hourglass-mode instabilities. We consider the Euler equations of gas dynamics in a Lagrangian

*Correspondence to: R. N. Rieben, Weapons and Complex Integration, Lawrence Livermore National Laboratory, 7000 East Ave L-095, Livermore, CA 94550, U.S.A.
†E-mail: rieben1@llnl.gov

Contract/grant sponsor: U.S. Department of Energy by Lawrence Livermore National Laboratory; contract/grant numbers: DE-AC52-07NA27344, LLNL-JRNL-422302.

frame given by

$$\text{Momentum conservation:} \quad \rho \frac{\mathrm{d}\vec{v}}{\mathrm{d}t} = -\vec{\nabla} p, \tag{1}$$

$$\text{Mass conservation:} \quad \frac{1}{\rho}\frac{\mathrm{d}\rho}{\mathrm{d}t} = -\vec{\nabla}\cdot\vec{v}, \tag{2}$$

$$\text{Energy conservation:} \quad \rho \frac{\mathrm{d}e}{\mathrm{d}t} = -p\vec{\nabla}\cdot\vec{v}, \tag{3}$$

$$\text{Equation of state:} \quad p = \text{EOS}\ (\rho, e), \tag{4}$$

where the EOS function defines the equation of state for a material, determining its pressure as a function of density and internal energy, see [1]. Note that the time derivatives are total derivatives moving with the flow and all spatial derivatives are taken with respect to a fixed coordinate system. Typically, these equations are solved on a staggered spatial grid [2, 3], where thermodynamic variables are approximated as piece-wise constants defined on zone centers, kinematic variables are defined on the nodes and spatial gradients are computed using finite volume and/or finite difference methods. Finite element discretizations have also been considered, in particular, see [4] and the references therein, where a low-order finite element scheme with mass lumping is proposed.

We propose a general finite element method (FEM) framework for solving the Euler equations in a moving material frame that has the following features:

1. Allows high-order field representations.
2. Support for quadrilateral/hexahedral as well as triangular/tetrahedral zone topologies.
3. Support for curvilinear zone geometries.
4. Exact energy conservation by construction.
5. Reduces to the classical SGH under simplifying assumptions.

In this paper, we review the key features of our general FEM approach (the theoretical details will be given in a forthcoming paper) and in particular, we consider a specific high-order method in 2D which we refer to as Q_2-$\widehat{Q}_1$ where kinematic variables and the computational mesh are defined using a continuous bi-quadratic basis and thermodynamic variables are defined using a discontinuous bi-linear basis.

2. SEMI-DISCRETE FINITE ELEMENT APPROXIMATION

Let $\Omega(t)$ be an arbitrary control volume (a set of particles) which deforms in time according to the velocity field $\vec{v}$ starting from an initial configuration, $\Omega(t_0)$. A semi-discrete Lagrangian method for (1)–(4) is concerned only with the spatial approximation of the continuum equations and begins with a discretization of the particle space, $\Omega(t)$. This means that the motion of the whole medium will be described by the motion of only a finite number of particles, see Figure 1.

2.1. Computational mesh and Lagrangian mesh motion

We decompose the spatial domain $\Omega(t)$ at the initial time $t = t_0$ into a set of non-overlapping, discrete volumes called zones (or elements), $\{\Omega_z(t_0)\}$. The union of these discrete zones forms the initial computational mesh, which we will denote with $\tilde{\Omega}(t_0)$, and is defined as

$$\Omega(t_0) \approx \tilde{\Omega}(t_0) \equiv \bigcup_z \Omega_z(t_0). \tag{5}$$

After deformation in time, the zones $\Omega_z(t)$ are reconstructed based on the locations of the particles associated with them (vertices, edge midpoints, etc.), thus defining the moved mesh $\tilde{\Omega}(t)$. Note that this reconstruction process introduces a *geometric error* (which should vanish under

DOI: 10.1002/fld

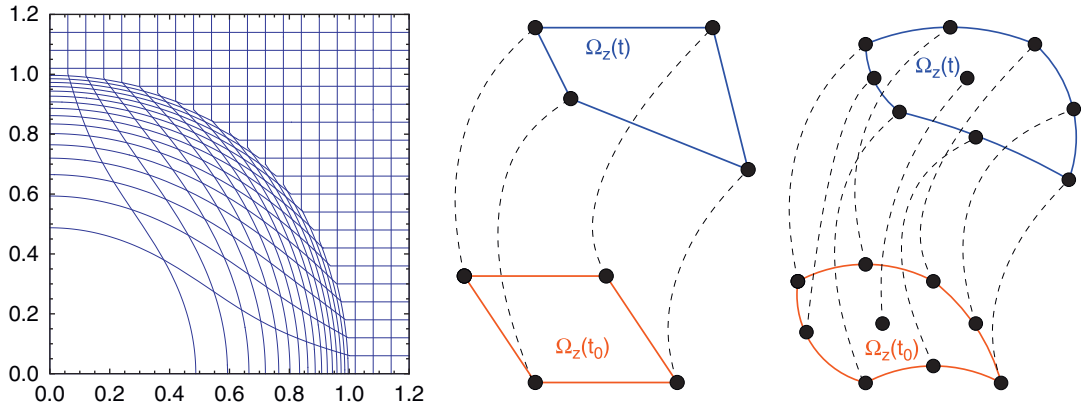

Figure 1. An initial Cartesian mesh is continuously deformed according to the exact solution of the Sedov blast wave (*left*). In a semi-discrete setting, a zone $\Omega_z(t)$ is reconstructed from the evolution of only a few of its points (particles) indicated by black dots. Shown are two specific choices corresponding to the traditional Q_1 zone (*center*) and a high-order Q_2 zone with curvilinear boundaries (*right*).

refinement), since the computational mesh $\tilde{\Omega}(t)$ will be only an approximation to the true geometry of the continuum domain $\Omega(t)$. As an example of this, consider Figure 1 where we begin with an initial 2D Cartesian mesh and continuously deform it according to the exact solution of the classical Sedov blast wave [5]. Note that the exact deformation field produces curvilinear boundaries between mesh zones. Using a traditional Q_1 (SGH) approximation for the kinematic variables will yield straight line zone boundaries. The presence of this built-in semi-discrete geometric error motivates the use of higher-order elements, such as the Q_2 element shown in Figure 1, since such elements have more degrees of freedom on the zone boundaries, allowing them to better represent continuous deformations.

2.2. *Curvilinear zone geometry*

We define the geometry of each Lagrangian zone, $\Omega_z(t)$, by a mapping from a standard reference zone, $\hat{\Omega}_z = [0,1]^2$, see Figure 2. This mapping is functionally written as

$$\vec{x} = \Phi(\hat{\vec{x}}, t), \tag{6}$$

where $\vec{x}$ denotes a point in the Lagrangian zone and $\hat{\vec{x}}$ denotes the corresponding point in the reference zone. This coordinate transformation is referred to as the parametric mapping and is defined by the Lagrangian coordinates of the particles associated with each zone. For the case of a traditional Q_1 zone geometry consisting of four vertices connected by straight lines, the parametric mapping is bi-linear. We propose to use high-order mappings such as Q_2 (bi-quadratic), which produce zones with curvilinear geometry as shown in Figure 2. Such mappings are computed for each zone using an interpolating polynomial expansion of the form

$$\Phi_z(\hat{\vec{x}}, t) = \sum_i \vec{x}_{z,i}(t)\eta_i(\hat{\vec{x}}), \tag{7}$$

where $\vec{x}_{z,i}(t)$ denote the Lagrangian coordinates of the particles describing the zone z at time t, see Figure 1, and η_i is the (high-order) nodal basis function associated with particle i. The collection of all particle coordinates, listed consecutively in a vector array, is denoted by $\mathbf{x}(t)$. We define the Jacobian matrix (or metric tensor) for this mapping as

$$\mathbf{J}_z = \vec{\nabla}_{\hat{\vec{x}}} \Phi_z \quad \text{or} \quad (\mathbf{J}_z)_{i,j} = \frac{\partial x_i}{\partial \hat{x}_j}. \tag{8}$$

Note that in general, the Jacobian matrix is a *function* of the reference coordinates $\hat{\vec{x}}$ and therefore varies in a zone.

DOI: 10.1002/fld

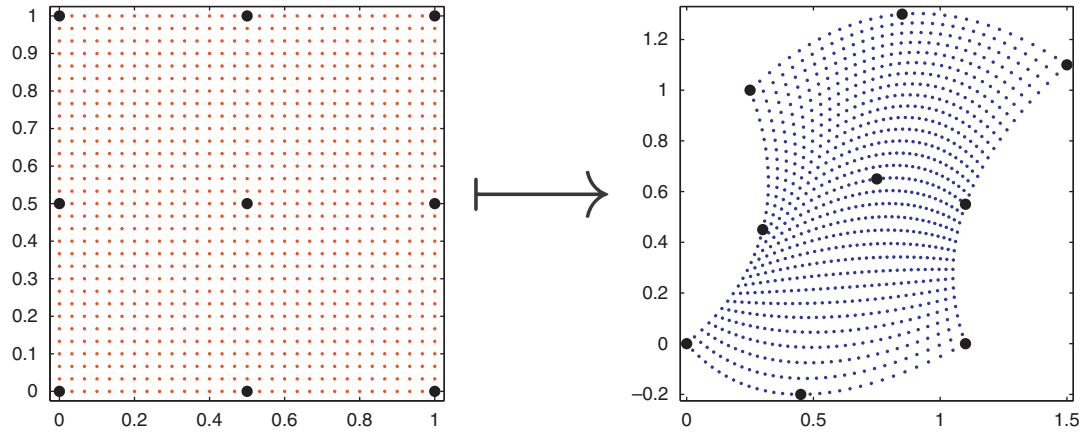

Figure 2. Example of a Q_2 bi-quadratic mapping from a reference zone (*left*) to a Lagrangian zone (*right*) defined by the locations of the nine Lagrangian particles (black dots).

2.3. High-order basis function expansions

In a traditional staggered grid approach, velocities are associated with zone vertices while densities, pressures and internal energies are treated as piece-wise constants associated with zone centers. In our general FEM approach, we assume that the fields $\vec{v}$, ρ, e and p are finite element functions on $\tilde{\Omega}(t)$ with the following expansions for $\vec{x} \in \tilde{\Omega}(t)$:

$$\vec{v}(\vec{x},t) \approx \sum_{i}^{N_{\mathbf{v}}} \mathbf{v}_i(t)\vec{w}_i(\vec{x},t), \tag{9}$$

$$\rho(\vec{x},t) \approx \sum_{i}^{N_{\mathbf{r}}} \mathbf{r}_i(t)\phi_i(\vec{x},t), \quad e(\vec{x},t) \approx \sum_{i}^{N_{\mathbf{e}}} \mathbf{e}_i(t)\phi_i(\vec{x},t), \quad p(\vec{x},t) \approx \sum_{i}^{N_{\mathbf{p}}} \mathbf{p}_i(t)\phi_i(\vec{x},t). \tag{10}$$

We pick the two components of the basis functions $\vec{w}_i$ to be the same as the nodal basis functions η_i in (7), while the thermodynamic variables use the discontinuous bi-linear basis ϕ_i, see Figure 3. These basis functions are defined to move with the mesh, such that they are constant along all particle trajectories. Therefore,

$$\frac{\mathrm{d}\vec{w}_i}{\mathrm{d}t} = \vec{0}, \quad \frac{\mathrm{d}\phi_i}{\mathrm{d}t} = 0. \tag{11}$$

Furthermore, the ordering of the vector $\mathbf{v}(t)$ coincides with that of the position vector $\mathbf{x}(t)$ from the previous section, and we have the equation of motion

$$\frac{\mathrm{d}\mathbf{x}}{\mathrm{d}t} = \mathbf{v}.$$

2.4. Semi-discrete momentum conservation

To derive a semi-discrete momentum conservation law, we begin by applying a variational formulation to the momentum conservation equation. We multiply (1) by a vector-valued test function $\vec{w}'$ and integrate over the spatial domain $\Omega(t)$ to get

$$\int_{\Omega(t)} \left(\rho \frac{\mathrm{d}\vec{v}}{\mathrm{d}t}\right) \cdot \vec{w}' = -\int_{\Omega(t)} (\vec{\nabla} p) \cdot \vec{w}'. \tag{12}$$

DOI: 10.1002/fld

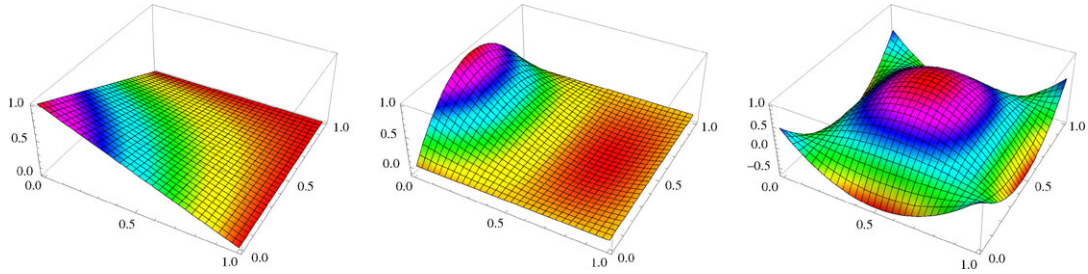

Figure 3. Examples of 2D basis functions on a reference zone: a standard Q_1 bi-linear function that interpolates at nodes (*left*), a Q_2 bi-quadratic function defined at the Gauss–Lobatto quadrature points (*center*) and a Q_2 bi-quadratic function defined at the Gauss–Legendre quadrature points (*right*).

Now, we replace the spatial domain $\Omega(t)$ with the (reconstructed) finite element mesh $\tilde{\Omega}(t)$. Performing integration by parts on the right-hand side of (12) and applying the divergence theorem, we obtain

$$\int_{\tilde{\Omega}(t)} \left(\rho \frac{\mathrm{d}\vec{v}}{\mathrm{d}t}\right) \cdot \vec{w}' = \int_{\tilde{\Omega}(t)} p(\vec{\nabla} \cdot \vec{w}') - \int_{\partial\tilde{\Omega}(t)} p(\vec{w}' \cdot \hat{n}), \tag{13}$$

where $\hat{n}$ is the outward pointing unit normal vector of the surface $\partial\tilde{\Omega}(t)$.

Inserting the discrete basis function expansions of (9) and (10) for the fields $\vec{v}$ and p, using (11), and assuming the boundary integral term vanishes (for the sake of brevity) give us

$$\int_{\tilde{\Omega}(t)} \left(\rho \sum_i^{N_\mathbf{v}} \frac{\mathrm{d}\mathbf{v}_i}{\mathrm{d}t} \vec{w}_i\right) \cdot \vec{w}' = \int_{\tilde{\Omega}(t)} \sum_i^{N_\mathbf{p}} \mathbf{p}_i \phi_i (\vec{\nabla} \cdot \vec{w}'). \tag{14}$$

Now, we apply Galerkin's method to the variational formulation (14), by picking the velocity basis functions $\vec{w}_j$ from (9) as our test function. This gives us the following linear system of ordinary differential equations (ODEs):

$$\sum_i^{N_\mathbf{v}} \frac{\mathrm{d}\mathbf{v}_i}{\mathrm{d}t} \int_{\tilde{\Omega}(t)} \rho(\vec{w}_i \cdot \vec{w}_j) = \sum_i^{N_\mathbf{p}} \mathbf{p}_i \int_{\tilde{\Omega}(t)} \phi_i (\vec{\nabla} \cdot \vec{w}_j). \tag{15}$$

In other words,

$$\boxed{\mathbf{M}\frac{\mathrm{d}\mathbf{v}}{\mathrm{d}t} = \mathbf{D}^\mathrm{T}\mathbf{p}} \quad , \tag{16}$$

where $\mathbf{M}, \mathbf{D}, \mathbf{v}$ and $\mathbf{p}$ are global matrices and vectors (or arrays) which are assembled over the entire mesh $\tilde{\Omega}(t)$ from the contributions of the degrees of freedom associated with each individual zone z as

$$\mathbf{M} = \text{Assemble}(\mathbf{M}_z), \quad \mathbf{D} = \text{Assemble}(\mathbf{D}_z),$$

$$\mathbf{v} = \text{Assemble}(\mathbf{v}_z), \quad \mathbf{p} = \text{Assemble}(\mathbf{p}_z).$$

The process of global assembly is analogous to the concept of 'nodal accumulation' that is used in a traditional SGH code, where a quantity at a node is defined to be the sum of contributions from all of the zones that share this node. Note that the presence of the global mass matrix $\mathbf{M}$ on the left-hand side of (16) means we must perform a linear solve to compute the accelerations.

The 'mass matrix' for a zone z at time t is simply

$$(\mathbf{M}_z)_{i,j} \equiv \int_{\Omega_z(t)} \rho(\vec{w}_i \cdot \vec{w}_j). \tag{17}$$

DOI: 10.1002/fld

This matrix is symmetric positive definite (SPD) by construction, and has a dimension 18×18. Furthermore, the vector nature of the basis $\{\vec{w}_j\}$ implies that $\mathbf{M}$ is block diagonal with identical $\mathbf{M}_{xx}$ and $\mathbf{M}_{yy}$ components of dimension 9×9. We define a 'discrete divergence', or 'derivative' matrix for zone z at time t as

$$(\mathbf{D}_z)_{i,j} \equiv \int_{\Omega_z(t)} \phi_i(\vec{\nabla} \cdot \vec{w}_j). \tag{18}$$

This matrix is *rectangular* with dimension 4×18. This rectangular derivative matrix is a map between the two discrete representations of velocity and pressure and is a discrete version of the Div operator. Its transpose is a discrete version of the Grad operator as seen in (16).

2.5. Calculating the mass and derivative matrices

In practice, the integrals for computing the mass and derivative matrices of (17) and (18) are calculated by transforming the integrals over each Lagrangian zone $\Omega_z(t)$ to the standard reference zone $\hat{\Omega}_z$ by using the parametric mapping of (6). Applying this transformation to a general integral over a given Lagrangian zone gives

$$\int_{\Omega_z(t)} f = \int_{\hat{\Omega}_z} (f \circ \Phi) |\det \mathbf{J}_z|,$$

for some integrand f, where '$\circ$' denotes composition. We approximate these integrals using a quadrature rule of a specified order. A general integral over a Lagrangian mesh zone is therefore replaced with a weighted sum of the form

$$\int_{\Omega_z(t)} f \approx \sum_{n=1}^{N_q} \alpha_n \{(f \circ \Phi) |\det \mathbf{J}_z|\}_{\hat{x}=\hat{q}_n}, \tag{19}$$

where α_n are the N_q quadrature weights and $\hat{\hat{q}}_n$ are quadrature points inside of the reference zone where the integrand is sampled at. Note that the use of quadrature in computing the integrals is not always exact (depending on the functional form of the integrand and the order of the quadrature rule), so we have introduced an additional approximation to the solution of the continuum equations. In practice, we use Gauss–Legendre quadrature rules on quadrilaterals. If we approximate the velocity using a piece-wise bi-linear basis (Q_1), the pressure using a piece-wise constant basis and we approximate the mass and derivative matrix integrals using the midpoint quadrature rule ($N_q = 1$), then it is straightforward to show that with these specific choices, we can exactly recover the traditional staggered-grid method of Wilkins [3] as well as a variant of the method described in [6].

2.6. Semi-discrete mass conservation

The fundamental assumption of the Lagrangian description of hydrodynamics is that the total mass of a given zone is a constant for all time

$$\frac{\mathrm{d}}{\mathrm{d}t} \int_{\Omega_z(t)} \rho = 0. \tag{20}$$

To facilitate high-order representations for the density field, we define high-order 'mass moments' for a given zone using the density basis functions from (10):

$$\mathbf{m}_{z,i} \equiv \int_{\Omega_z(t)} \rho \phi_i. \tag{21}$$

We generalize the case of zonal mass conservation to the high-order mass moments by postulating that

$$\frac{\mathrm{d}\mathbf{m}_{z,i}}{\mathrm{d}t} = 0. \tag{22}$$

DOI: 10.1002/fld

This choice is motivated by the fact that the same equation holds in the continuous case. Furthermore, (22) has the same number of conditions as the number of unknown densities and in particular it implies (20). Note that for the case of a piece-wise constant density approximation (a single mass moment), we recover the traditional definition of zonal mass conservation. Substituting the basis function representation of the density field (10) in (21) we get the matrix equation

$$\mathbf{m}_z = \mathbf{M}_z^\rho \mathbf{r}_z \quad \text{where } (\mathbf{M}_z^\rho)_{i,j} \equiv \int_{\Omega_z(t)} \phi_i \phi_j.$$

This yields the semi-discrete mass conservation law

$$\boxed{\frac{\mathrm{d}}{\mathrm{d}t}(\mathbf{M}_z^\rho \mathbf{r}_z) = 0}. \tag{23}$$

The above can be viewed as a generalization of the 'sub-zonal mass' concept introduced in [7]; it is a statement that no mass enters or leaves a given sub-volume of the zone. If we take the limiting case of this idea and impose mass conservation of the form

$$\frac{\mathrm{d}}{\mathrm{d}t} \int_{\Omega'(t)} \rho = 0 \quad \text{for any } \Omega'(t) \subseteq \Omega_z(t),$$

then we obtain the *strong mass conservation principle*

$$\rho(t) |\det \mathbf{J}_z(t)| = \rho(t_0) |\det \mathbf{J}_z(t_0)| \tag{24}$$

which is a statement of mass conservation for any point in space (not just in a variational sense). Note that the density defined by this equation is not polynomial.

We can write the following relation between the finite element density function defined by (23) and the function defined by (24) (denoted here by ρ_h and ρ_s, respectively):

$$\int_{\Omega_z(t)} \rho_h \phi_i = \int_{\Omega_z(t)} \rho_s \phi_i, \tag{25}$$

which tells us that ρ_h is the projection of ρ_s on the space spanned by $\{\phi_i\}$.

2.7. Semi-discrete energy conservation

To derive a semi-discrete energy conservation law, we consider a local variational formulation of the energy conservation equation (3)

$$\int_{\Omega_z(t)} \rho \frac{\mathrm{d}e}{\mathrm{d}t} \phi_j = \int_{\Omega_z(t)} p(\vec{\nabla} \cdot \vec{v}) \phi_j.$$

Inserting the basis function expansions for internal energy, pressure and velocity we obtain

$$\boxed{\mathbf{M}_z^e \frac{\mathrm{d}\mathbf{e}_z}{\mathrm{d}t} = -\mathbf{p}_z \cdot \mathbf{D}_z^e \cdot \mathbf{v}_z} \tag{26}$$

where

$$(\mathbf{M}_z^e)_{i,j} \equiv \int_{\Omega_z(t)} \rho \phi_i \phi_j \quad \text{and} \quad (\mathbf{D}_z^e)_{i,j,k} \equiv \int_{\Omega_z(t)} \phi_i \phi_j (\vec{\nabla} \cdot \vec{w}_k).$$

Here $\mathbf{D}_z^e$ is tensor of rank 3 satisfying $\mathbf{D}_z = \mathbf{D}_z^e \cdot \mathbf{1}_z^e$, i.e. $(\mathbf{D}_z)_{i,k} = \sum_j (\mathbf{D}_z^e)_{i,j,k} (\mathbf{1}_z^e)_j$, where $\mathbf{1}_z^e$ is the zonal representation of the constant 1 in the internal energy space (a vector of ones for nodal finite elements). In this formulation, the matrix $\mathbf{F}_z = \mathbf{p}_z \cdot \mathbf{D}_z^e$ can be used to generalize the concept of 'corner forces' (see below), since $\mathbf{F}_z^{\mathrm{T}} \cdot \mathbf{1}_z^e$ gives the zonal forces in the momentum equation, while $\mathbf{F}_z \cdot \mathbf{v}_z$ is the work term due to the pressure gradient forces.

DOI: 10.1002/fld

Given the above definitions, we can show that the following semi-discrete energy conservation relation holds:

$$\frac{\mathrm{d}\tilde{E}}{\mathrm{d}t}=\frac{\mathrm{d}}{\mathrm{d}t}\left(\frac{1}{2}\mathbf{v}\cdot\mathbf{M}\cdot\mathbf{v}+\sum_z \mathbf{1}_z^e\cdot\mathbf{M}_z^e\cdot\mathbf{e}_z\right)=\frac{1}{2}\mathbf{v}\cdot\frac{\mathrm{d}\mathbf{M}}{\mathrm{d}t}\cdot\mathbf{v}+\sum_z \mathbf{1}_z^e\cdot\frac{\mathrm{d}\mathbf{M}_z^e}{\mathrm{d}t}\cdot\mathbf{e}_z, \tag{27}$$

where $\tilde{E}$ denotes the total discrete energy in the computational domain. Note that there is both a kinetic energy term and an internal energy term and that the time rate of change of this sum is equal to zero (implying total energy conservation) when the time derivatives of the mass matrices $\mathbf{M}$ and $\mathbf{M}_z^e$ are zero. For the case where the mass matrices change in time (implying a redistribution of mass within a zone), this change must be taken into account in order to maintain exact energy conservation.

For the special case of piece-wise constant internal energies (i.e. a single constant basis function) and a single zonal mass, $\mathbf{m}_z$, Equation (26) reduces to the form

$$\mathbf{m}_z\frac{\mathrm{d}\mathbf{e}_z}{\mathrm{d}t}=-\mathbf{p}_z\mathbf{D}_z\mathbf{v}_z. \tag{28}$$

The term $\mathbf{p}_z\mathbf{D}_z$ is simply a collection of 'corner forces' due to the discrete pressure gradient term and therefore

$$(\mathbf{p}_z\mathbf{D}_z)\mathbf{v}_z=\sum_i \vec{f}_i\cdot\vec{v}_i.$$

Thus, Equation (26) can be viewed as a generalization of the so-called 'compatible hydro' approach of [7], which was also applied in a FEM context in [4, 8].

2.8. Equation of state

The equation of state can be computed point-wise at the pressure degrees of freedom, or it can also be considered in a weak form. For example, the variational form of the gamma-law $p=(\gamma-1)\rho e$ is

$$\int_{\Omega_z(t)} p\phi_j=\int_{\Omega_z(t)}(\gamma-1)\rho e\phi_j.$$

In matrix form, this reads (for γ constant in a zone)

$$\boxed{\mathbf{M}_z^\rho\mathbf{p}_z=(\gamma-1)\mathbf{M}_z^e\mathbf{e}_z} \tag{29}$$

3. FULLY DISCRETE FINITE ELEMENT APPROXIMATION

In a fully discrete approximation, we also discretize in time. In this paper, for the purposes of illustration, we consider the simple case of a forward Euler-like scheme.

3.1. Fully discrete momentum and energy conservation

Applying the forward Euler time integration scheme to the semi-discrete momentum conservation of (16) yields

$$\boxed{\mathbf{M}^{n+1}\mathbf{v}^{n+1}=\mathbf{M}^n\mathbf{v}^n+\Delta t(\mathbf{D}^n)^{\mathrm{T}}\mathbf{p}^n}$$

Note that under the strong mass conservation principle of (24), the mass matrix $\mathbf{M}^n=\mathbf{M}$ is a constant for all time and therefore only needs to be computed once. Furthermore, the change in kinetic energy over a time step Δt is given by

$$\tfrac{1}{2}(\mathbf{v}^{n+1})^{\mathrm{T}}\mathbf{M}\mathbf{v}^{n+1}-\tfrac{1}{2}(\mathbf{v}^n)^{\mathrm{T}}\mathbf{M}\mathbf{v}^n=(\mathbf{v}^{n+\frac{1}{2}})^{\mathrm{T}}\mathbf{M}(\mathbf{v}^{n+1}-\mathbf{v}^n)=\Delta t\mathbf{v}^{n+\frac{1}{2}}(\mathbf{D}^n)^{\mathrm{T}}\mathbf{p}^n,$$

DOI: 10.1002/fld

where $\mathbf{v}^{n+\frac{1}{2}} \equiv (\mathbf{v}^{n+1} + \mathbf{v}^n)/2$. Thus, in order to preserve the total discrete energy exactly from time step n to time step $n+1$, the energy update should have the form

$$\boxed{\mathbf{M}_z^{e,n+1}\mathbf{e}_z^{n+1} = \mathbf{M}_z^{e,n}\mathbf{e}_z^n - \Delta t\, \mathbf{p}_z^n \cdot \mathbf{D}_z^{e,n} \cdot \mathbf{v}_z^{n+\frac{1}{2}}} \tag{30}$$

which is a discretization of (26).

3.2. Fully discrete mass conservation and equation of state

Based on the semi-discrete mass conservation equation (23), we update density using

$$\mathbf{M}_z^{\rho,n+1}\mathbf{r}_z^{n+1} = \mathbf{M}_z^{\rho,n}\mathbf{r}_z^n = \cdots = \mathbf{M}_z^{\rho,0}\mathbf{r}_z^0 = \mathbf{m}_z^0. \tag{31}$$

In other words,

$$\boxed{\mathbf{M}_z^{\rho,n+1}\mathbf{r}_z^{n+1} = \mathbf{m}_z^0} \tag{32}$$

Our discretization of the equation of state remains unchanged from the semi-discrete case (29) and we apply it at every discrete time step

$$\boxed{\mathbf{M}_z^{\rho,n+1}\mathbf{p}_z^{n+1} = (\gamma - 1)\mathbf{M}_z^{e,n+1}\mathbf{e}_z^{n+1}}$$

3.3. Artificial viscosity

To handle shock waves, we use the tensor artificial viscosity formulation of [9]. In this formulation, it is straightforward to adapt the artificial force and energy (or shock heating) terms for the case of high-order velocity field representations. To summarize the approach, we augment the momentum and energy conservation equations of (1) and (3) with a generalized viscous force and corresponding energy term

$$\rho\frac{\mathrm{d}\vec{v}}{\mathrm{d}t} = -\vec{\nabla}p + \vec{\nabla}\cdot(\mu\vec{\nabla}\vec{v}), \quad \rho\frac{\mathrm{d}e}{\mathrm{d}t} = -p\vec{\nabla}\cdot\vec{v} + (\mu\vec{\nabla}\vec{v}) : (\vec{\nabla}\vec{v}).$$

Applying a variational formulation to the momentum equation and using the (high-order) velocity basis functions, we compute for every zone the local forces (analogous to corner forces)

$$\mathbf{f}_z = \mathbf{S}_z\mathbf{v}_z \quad \text{where } (\mathbf{S}_z)_{i,j} = \int_{\Omega_z(t)} (\mu_z\vec{\nabla}\vec{w}_i) : \vec{\nabla}\vec{w}_j. \tag{33}$$

Note that, similarly to the mass matrix, the stiffness matrix $\mathbf{S} = \text{Assemble}(\mathbf{S}_z)$ is block diagonal with $\mathbf{S}_{xx} = \mathbf{S}_{yy}$. Furthermore, in the general case, the zone-based artificial viscosity coefficient μ_z is a function of space. The corresponding work due to the artificial viscosity is given by the inner product

$$\Delta\mathbf{e}_z = \mathbf{v}_z \cdot \mathbf{S}_z^e \cdot \mathbf{v}_z \quad \text{where } (\mathbf{S}_z^e)_{i,j,k} = \int_{\Omega_z(t)} (\mu_z\vec{\nabla}\vec{w}_i) : (\vec{\nabla}\vec{w}_k)\phi_j,$$

and we have $\mathbf{S}_z = \mathbf{S}_z^e \cdot \mathbf{1}_z^e$. In practice, we compute the viscosity coefficient μ_z as a function which is sampled at the quadrature points of the integral in (33); μ_z has a form similar to that described in [9] including both linear and quadratic diffusion terms.

Note that we use an artificial stress term of the form $\sigma_a = \mu\vec{\nabla}\vec{v}$, which is generally not symmetric and therefore conservation of angular momentum can be violated on a continuous level. For problems where $\vec{\nabla}\vec{v}$ is not symmetric, implying $\vec{\nabla}\times\vec{v} \neq 0$, one can use the form $\sigma_a = \mu(\vec{\nabla}\vec{v} + \vec{v}\vec{\nabla})/2$ instead, cf. [4]. The generalization of $\mathbf{S}_z$ and $\mathbf{S}_z^e$ to this or other forms of σ_a is straightforward.

DOI: 10.1002/fld

3.4. Fully discrete scheme

We use the strong mass conservation principle (24) which, as previously stated, lets us avoid re-computing the velocity mass matrix $\mathbf{M}^n = \mathbf{M}$ and the energy matrices $\mathbf{M}_z^{e,n} = \mathbf{M}_z^e$ (note that the time independence of $\mathbf{M}$ and $\mathbf{M}_z^e$ was previously used in [4] where $\mathbf{M}$ is additionally lumped and $\mathbf{M}_z^e$ is just a scalar.) To summarize, the overall computational scheme is

$$\begin{aligned}
\mathbf{F}^n &= \mathbf{p}^n \cdot \mathbf{D}^{e,n} - \mathbf{v}^n \cdot \mathbf{S}^{e,n}, \\
\mathbf{M}\mathbf{v}^{n+1} &= \mathbf{M}\mathbf{v}^n + \Delta t (\mathbf{F}^n)^{\mathrm{T}} \cdot \mathbf{1}^e, \\
\mathbf{M}_z^{\rho,n+1} \mathbf{r}_z^{n+1} &= \mathbf{m}_z^0, \\
\mathbf{M}_z^e \mathbf{e}_z^{n+1} &= \mathbf{M}_z^e \mathbf{e}_z^n - \Delta t \mathbf{F}_z^n \cdot \mathbf{v}_z^{n+\frac{1}{2}}, \\
\mathbf{M}_z^{\rho,n+1} \mathbf{p}_z^{n+1} &= (\gamma - 1) \mathbf{M}_z^e \mathbf{e}_z^{n+1}.
\end{aligned}$$

In the above algorithm, we first compute $\mathbf{F}^n$ by assembling the generalized 'corner forces'

$$(\mathbf{F}_z^n)_{i,j} = \int_{\Omega_z(t_n)} (p^n I - \mu_z^n \vec{\nabla} \vec{v}^n) : \vec{\nabla} \vec{w}_i \phi_j$$

on the current mesh Ω^n. After solving the momentum conservation equation, the mesh is moved $\Omega^n \mapsto \Omega^{n+1}$ using the new velocity by updating the Q_2 degrees of freedom:

$$\mathbf{x}^{n+1} = \mathbf{x}^n + \Delta t \mathbf{v}^{n+1}.$$

The equations involving the thermodynamic variables are local, and the zonal mass matrices can be made diagonal through a proper choice of basis functions and quadrature rules.

4. NUMERICAL RESULTS

We now present a series of numerical results using the proposed 2D curvilinear method. In each example, we use the tensor artificial viscosity formulation where the coefficient μ_z has a linear term scaling of $q_{\mathrm{lin}} = \frac{1}{4}$, a quadratic term scaling of $q_{\mathrm{quad}} = \frac{2}{3}$ and a local length scale that is directionally based (similar to 'model 3' in [9]). We follow the algorithm of Section 3.4 and for each time step we solve the global momentum equation using a simple preconditioned conjugate gradient algorithm with a relative residual tolerance of 10^{-8}. We note that there is no 'hourglass' filtering or treatment used in these examples.

4.1. Sod shock tube

We begin with a simple 1D Riemann problem, the Sod shock tube with $\gamma = \frac{5}{3}$ and initial states $\rho_L = 1.0$, $p_L = 1$ and $\rho_R = 0.125$, $p_R = 0.1$. In Figure 4, we plot results for the velocity, density, internal energy and pressure at the final time of $t = 0.2$ using a sequence of 'one-dimensional' meshes consisting of 50, 100 and 200 zones in the x direction and a single zone in the y direction. For each plot, the fields are sampled uniformly using the basis function expansions of (9)–(10) with 10 plot points per zone. Note that since we are using a high-order method, we have essentially doubled the resolution of a standard Q_1 method for a given mesh. For reference, we also include results generated with a traditional Q_1 SGH code. Because we are using a discontinuous basis for the thermodynamic variables, we capture the material contact discontinuity without any diffusion. We observe the 'wall heating' phenomenon in the internal energy and its subsequent effect on the density at the contact. In Figure 5, we show plots of the velocity and density zoomed in around the shock front. Here, we can more clearly see the convergence of the solution under mesh refinement, the smooth quadratic variation in the velocity and the discontinuous linear nature of the density.

DOI: 10.1002/fld

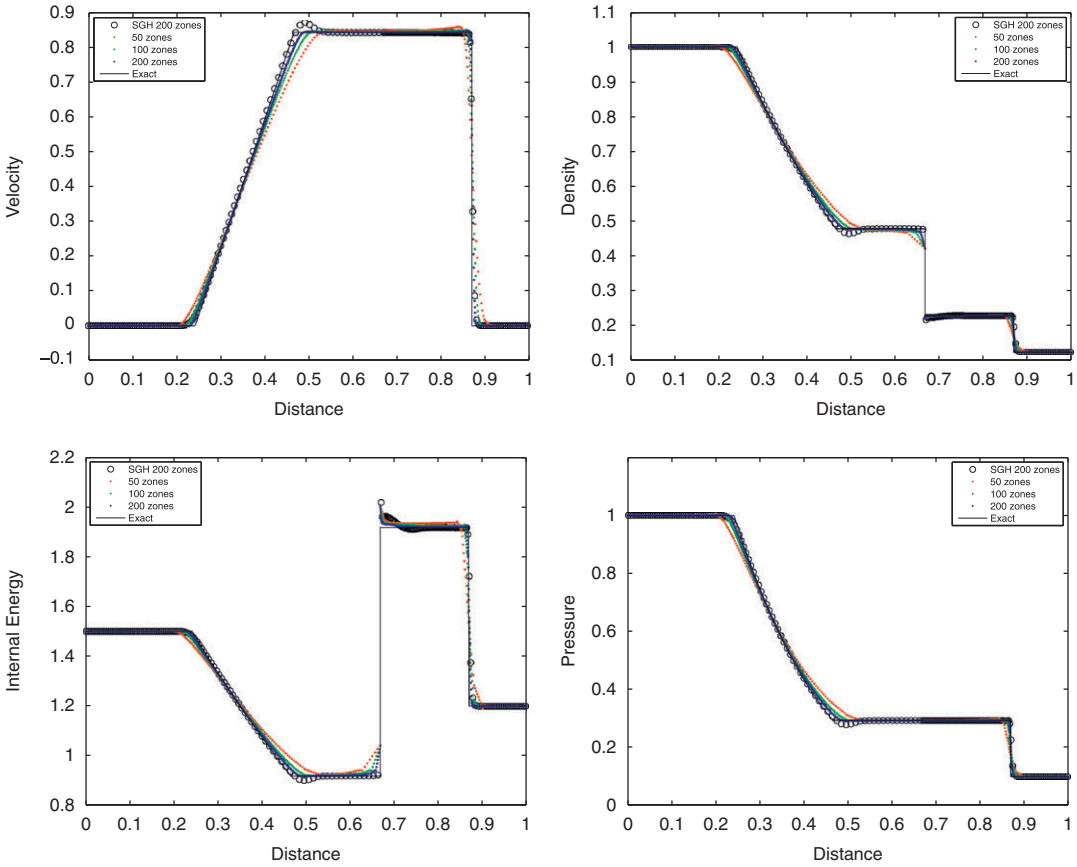

Figure 4. Results for the Sod shock tube on a 50, 100 and 200 zone mesh (along with a reference SGH result on 200 zones): velocity (*top-left*), density (*top-right*), internal energy (*bottom-left*) and pressure (*bottom-right*),

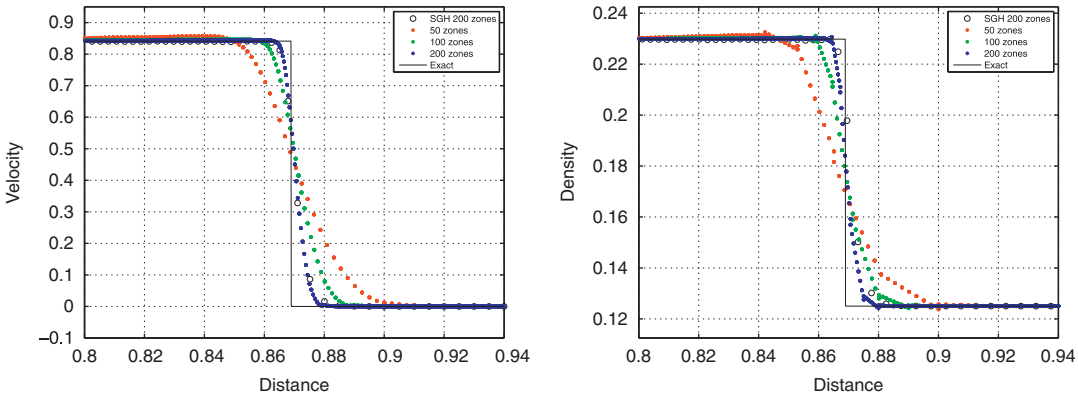

Figure 5. Results for the Sod shock tube on a 50, 100 and 200 zone mesh (along with a reference SGH result on 200 zones), zoomed in around the shock front illustrating the quadratic velocity (*left*) and discontinuous linear density (*right*).

4.2. Noh implosion

Next, we consider the Noh implosion test problem [10] in planar x–y coordinates on an initially Cartesian mesh of the domain $[-1,1]\times[-1,1]$. The problem consists of an ideal gas with $\gamma=\frac{5}{3}$, initial density $\rho_0=1$ and initial energy $e_0=0$. The value of each Q_2 velocity degree of freedom is

DOI: 10.1002/fld

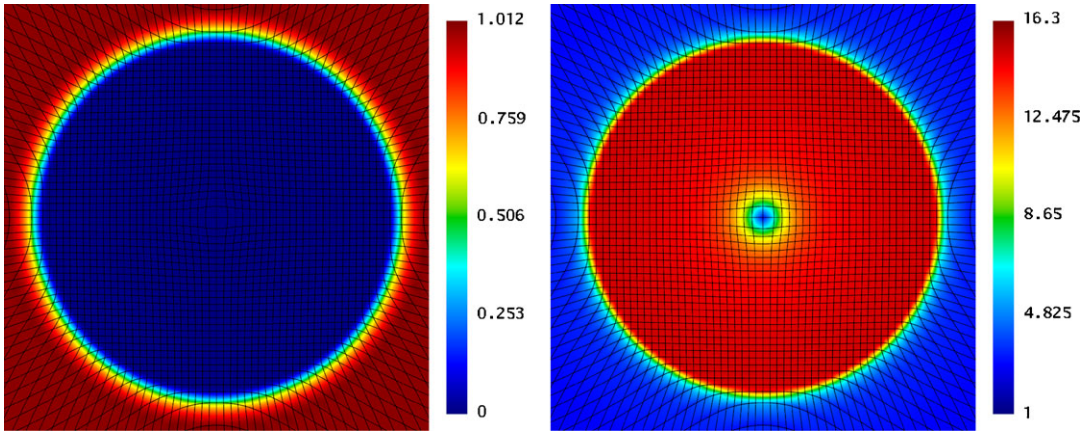

Figure 6. Curvilinear mesh at $t = 0.6$ and pseudo-color plots of velocity (*left*) and density (*right*) for the Noh problem on an initial 64×64 zone Cartesian mesh of the domain $[-1, 1] \times [-1, 1]$.

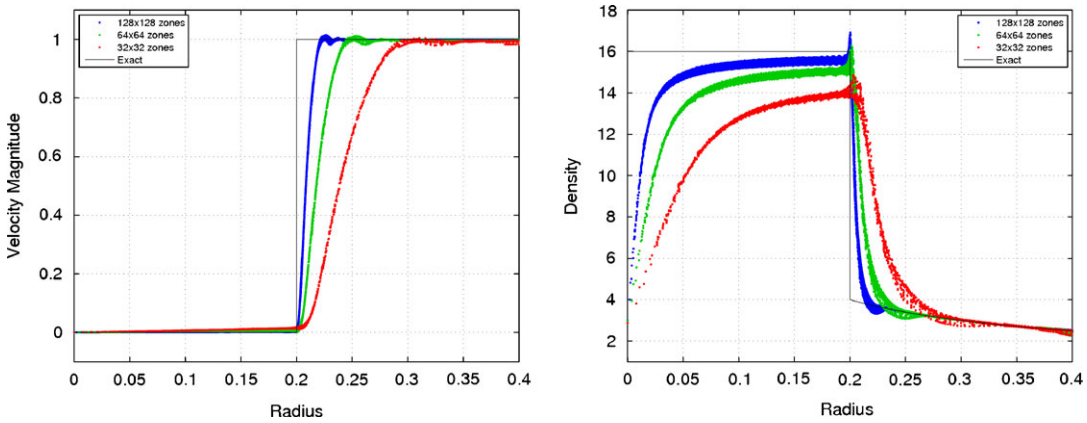

Figure 7. Scatter plots (25 points per zone) of velocity magnitude (*left*) and density (*right*) for the Noh problem on an initial 128×128, 64×64 and 32×32 zone Cartesian mesh of the domain $[-1, 1] \times [-1, 1]$.

initialized to a radial vector pointing toward the origin, $\vec{v} = -\vec{r}/\|\vec{r}\|$. The initial velocity generates a stagnation shock wave that propagates radially outward and produces a peak postshock density of $\rho = 16$. In Figure 6, we show plots of the curvilinear mesh along with the velocity and density fields sampled with 8×8 uniform sub-divisions per zone. Note the excellent radial symmetry of the fields and mesh. In Figure 7, we show scatter plots of the velocity and density fields sampled at 25 points per zone on a sequence of refined meshes, demonstrating the convergence of the method. Note that in each case, the shock is effectively resolved in two zones, where the overshoots occur when the solution is sampled near the postshock zone boundaries and the undershoots occur when the solution is sampled near the preshock zone boundaries. We note that the magnitude of such overshoots/undershoots does not diminish under mesh refinement with our current method. Finally, in Figure 8 we show a comparison of the computed and the exact position of 25 particles per zone and their corresponding errors.

4.3. Sedov blast wave

Here, we consider the Sedov explosion test problem [5] in planar x–y geometry. The problem consists of an ideal gas ($\gamma = 1.4$) with a delta function source of internal energy deposited at the origin. The sudden release of the energy creates an expanding shock wave, converting the initial internal energy into kinetic energy. The delta function energy source is approximated by setting

DOI: 10.1002/fld

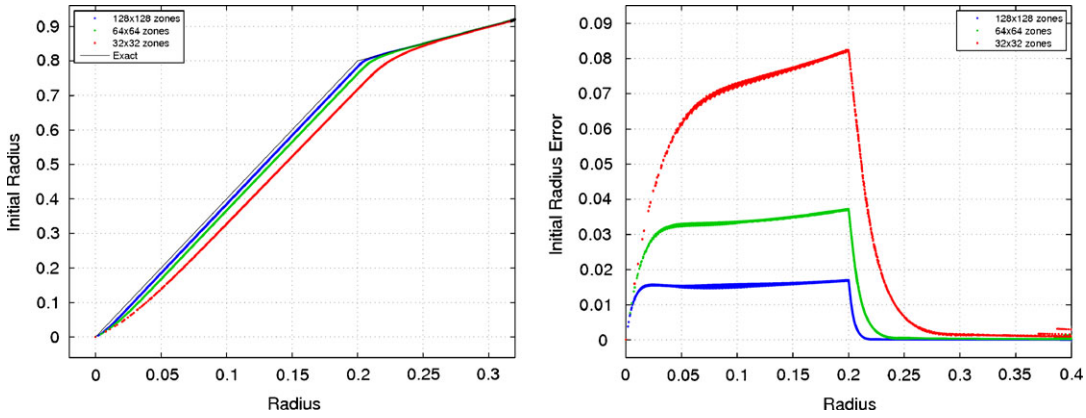

Figure 8. Scatter plots (25 points per zone) of initial radius (*left*) and its error (*right*) for the Noh problem on an initial 128×128, 64×64 and 32×32 zone Cartesian mesh of the domain $[-1,1]\times[-1,1]$.

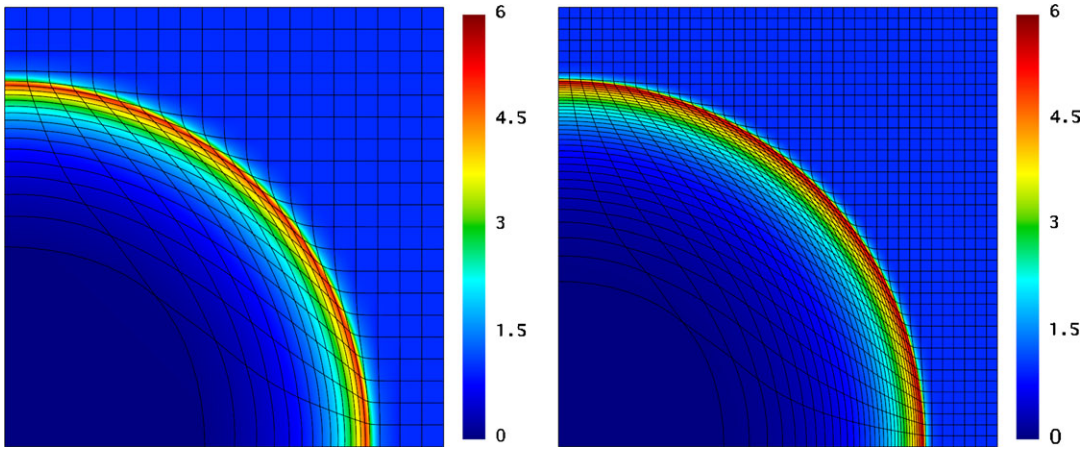

Figure 9. Curvilinear mesh at $t=1.0$ and pseudo-color plots of density for the Sedov problem on an initial 20×20 (*left*) and 40×40 (*right*) zone Cartesian mesh of the domain $[0,1.2]\times[0,1.2]$.

the values of e_0 to zero in all vertices except at the origin where the value is chosen so that the total internal energy is $\frac{1}{4}$. In Figure 9, we show plots of the curvilinear mesh and the density field sampled with 8×8 uniform sub-divisions per zone for 20×20 and 40×40 zone meshes. Note the curved mesh boundaries and compare to the exact case of Figure 1 as well as the excellent radial symmetry of the fields and mesh. In Figure 10, we show scatter plots of the density field sampled at 25 points per zone compared with the exact solution. Note that in this case, the shock is effectively resolved in a single zone. In Figure 11, we show scatter plots of the initial radial location of each point vs the current radius and compare to the exact solution. In both the cases we also compare to a solution generated with a traditional Q_1 SGH on meshes with an equivalent degree of freedom count.

We conclude by demonstrating the potential of the method on a highly distorted mesh, given by applying the following two-step transformation to an initial Cartesian mesh, see Figure 12.

(1) Given initial coordinates (x_0, y_0) with their corresponding polar coordinates (r_0, θ_0), we define

$$r_1 = 1.2\tilde{r}_0 \quad \text{and} \quad \theta_1 = \theta_0 + \frac{\pi}{3}\cos\left(\frac{\pi}{2}\tilde{r}_0\right) \quad \text{where } \tilde{r}_0 = \max\{|x_0|, |y_0|\}.$$

DOI: 10.1002/fld

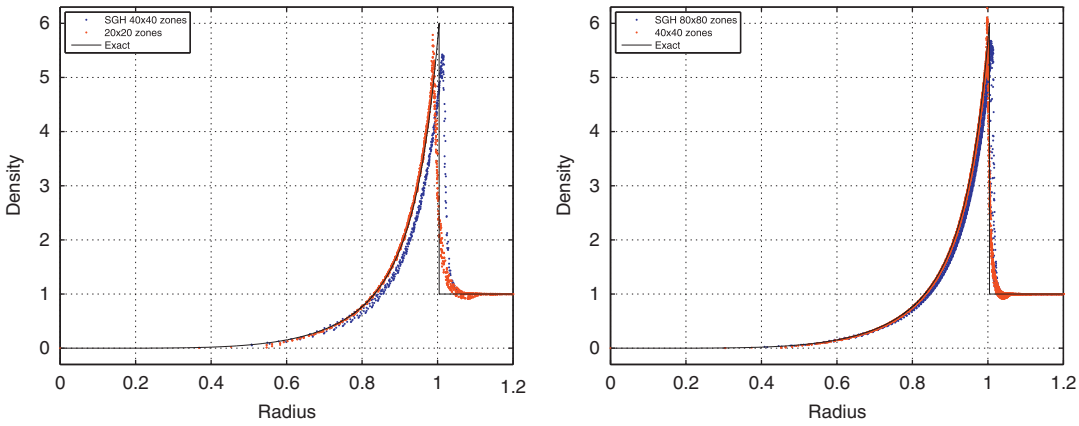

Figure 10. Scatter plots (9 points per zone) of density (along with a reference SGH result) for the Sedov problem on an initial 20×20 (*left*) and 40×40 (*right*) zone Cartesian mesh of the domain $[0, 1.2]\times[0, 1.2]$.

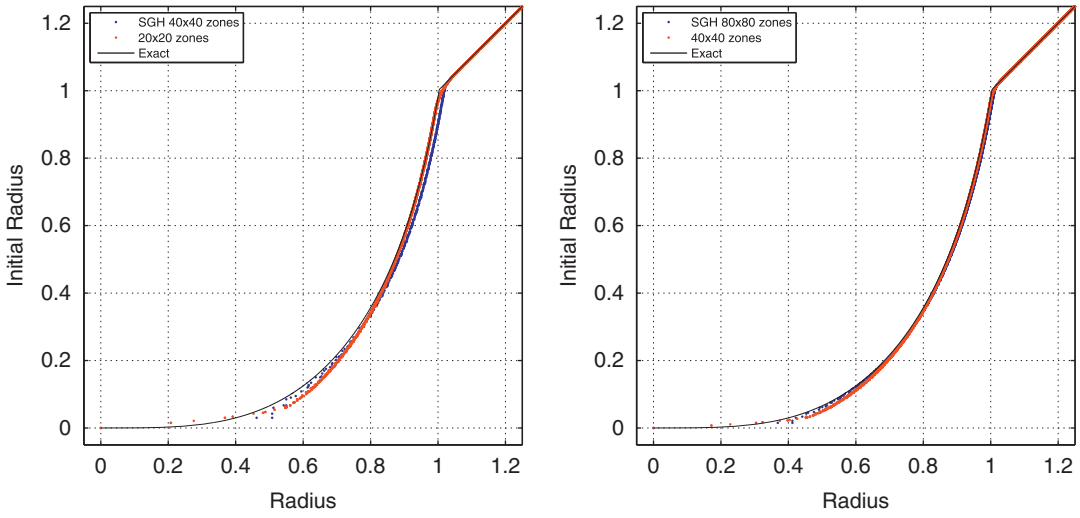

Figure 11. Scatter plots (25 points per zone) of initial radius (along with a reference SGH result) for the Sedov problem on an initial 20×20 (*left*) and 40×40 (*right*) zone Cartesian mesh of the domain $[0, 1.2]\times[0, 1.2]$.

(2) Let (x_1, y_1) be the Cartesian coordinates of (r_1, θ_1). The final position of (x_0, y_0) is

$$\begin{pmatrix} x_2 \\ y_2 \end{pmatrix} = U\Lambda U^t \begin{pmatrix} x_1 \\ y_1 \end{pmatrix} \quad \text{where } \Lambda = \begin{pmatrix} \dfrac{1+\sqrt{5}}{2} & 0 \\ 0 & 1 \end{pmatrix}, \quad U = \begin{pmatrix} \cos\alpha & \sin\alpha \\ -\sin\alpha & \cos\alpha \end{pmatrix}, \quad \alpha = \frac{\pi}{6}.$$

We run the Sedov problem on a grid obtained by applying the above transformation to a 64×64 mesh on $[-1, 1]\times[-1, 1]$. In this test, we use a simpler version of the viscosity coefficient μ_z, where the local length scale is not directionally based. The results, presented in Figure 13, demonstrate that our method preserves radial symmetry, even on this highly distorted mesh, which contains nearly singular elements with angles close to π.

DOI: 10.1002/fld

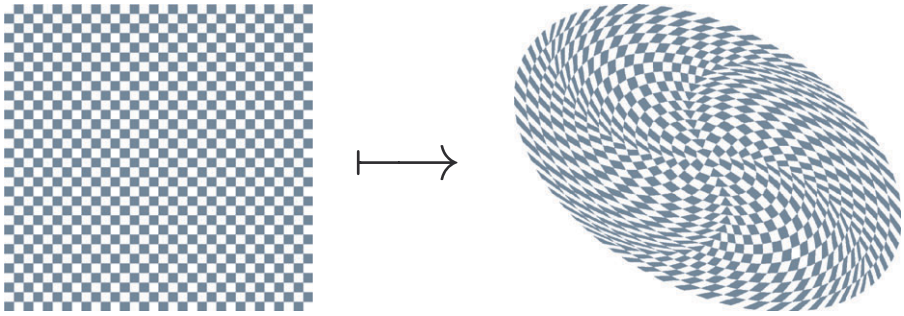

Figure 12. Illustration of the transformation used to define the distorted mesh.

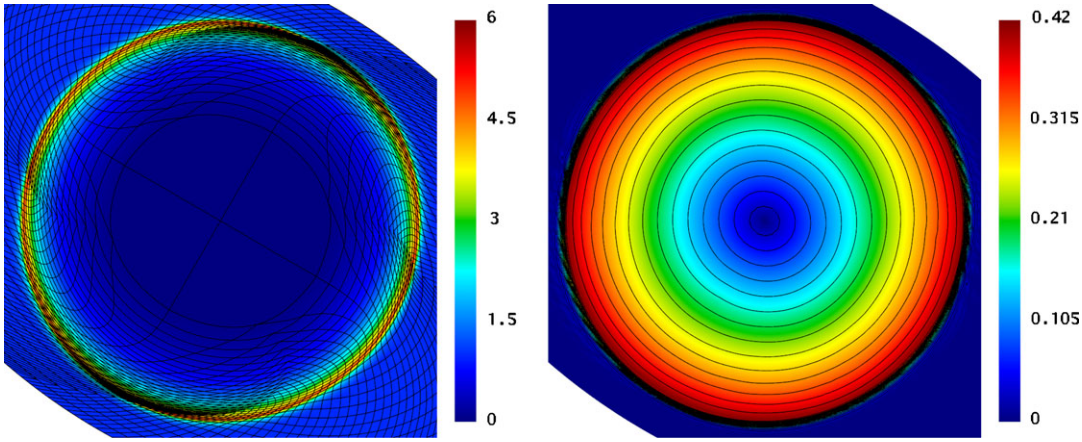

Figure 13. Results for the Sedov problem on a 64×64 distorted grid at $t = 1.0$. Curvilinear mesh and pseudo-color plot of density (*left*) and a contour plot of the velocity magnitude (*right*).

5. CONCLUSIONS

We have developed and presented a curvilinear finite element method for Lagrangian hydrodynamics which is derived from our general high-order energy conserving framework. We have demonstrated via numerical examples the benefits that can be obtained by using such a method. Finally, we feel that even more significant benefits of such a method will be realized by exploring problems with more complicated initial geometries.

ACKNOWLEDGEMENTS

This paper performed under the auspices of the U.S. Department of Energy by Lawrence Livermore National Laboratory under Contract DE-AC52-07NA27344, LLNL-JRNL-422302.

REFERENCES

1. Ockendon H, Ockendon J. *Waves and Compressible Flow*. Texts in Applied Mathematics, vol. 47. Springer: Berlin, 2004.
2. Tipton R. CALE Lagrange step. *Technical Report*, vol. 47, Lawrence Livermore National Laboratory, October 1990.
3. Wilkins ML. *Methods in Computational Physics*, *Calculation of Elastic-plastic Flow*. Academic Press: New York, 1964.
4. Scovazzi G, Love E, Shashkov M. Multi-scale Lagrangian shock hydrodynamics on Q1/P0 finite elements: Theoretical framework and two-dimensional computations. *Computer Methods in Applied Mechanics and Engineering* 2008; **197**:1056–1079.

DOI: 10.1002/fld

5. Sedov LI. *Similarity and Dimensional Methods in Mechanics* (10th edn). CRC Press: Boca Raton, 1993.
6. Caramana EJ, Shashkov MJ. Elimination of artificial grid distortion and hourglass-type motions by means of Lagrangian subzonal masses and pressures. *Journal of Computational Physics* 1998; **142**(2):521–561.
7. Caramana EJ, Burton DE, Shashkov MJ, Whalen PP. The construction of compatible hydrodynamics algorithms utilizing conservation of total energy. *Journal of Computational Physics* 1998; **146**:227–262.
8. Barlow A. A compatible finite element multi-material ALE hydrodynamics algorithm. *International Journal for Numerical Methods in Fluids* 2007; **56**:953–964.
9. Kolev TzV, Rieben RN. A tensor artificial viscosity using a finite element approach. *Journal of Computational Physics* 2009; **228**(22):8336–8366.
10. Noh WF. Errors for calculations of strong shocks using an artificial viscosity and an artificial heat flux. *Journal of Computational Physics* 1987; **72**(1):78–120.

DOI: 10.1002/fld